

pubsiacs.org/Nanol ett Letter

Manipulating Interlayer Excitons for Near-Infrared Quantum Light Generation

Huan Zhao,* Linghan Zhu, Xiangzhi Li, Vigneshwaran Chandrasekaran, Jon Kevin Baldwin, Michael T. Pettes, Andrei Piryatinski, Li Yang,* and Han Htoon*



Cite This: Nano Lett. 2023, 23, 11006-11012



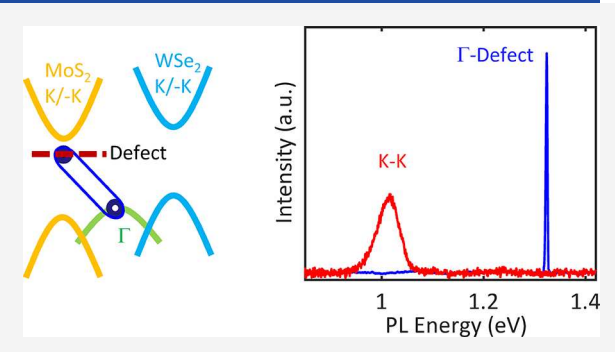
ACCESS I

Metrics & More

Article Recommendations

Supporting Information

ABSTRACT: Interlayer excitons (IXs) formed at the interface of van der Waals materials possess various novel properties. In parallel development, strain engineering has emerged as an effective means for creating 2D quantum emitters. Exploring the intersection of these two exciting areas, we use MoS₂/WSe₂ heterostructure as a model system and demonstrate how strain, defects, and layering can be utilized to create defect-bound IXs capable of bright, robust, and tunable quantum light emission in the technologically important near-infrared spectral range. Our work presents defect-bound IXs as a promising platform for pushing the performance of 2D quantum emitters beyond their current limitations.



KEYWORDS: interlayer exciton, TMDC, 2D heterostructures, quantum emitters

terobilayers (HBLs) of transition metal dichalcogenides (TMDCs) with staggered type-II band alignment are particularly fascinating as they allow the formation of chargeseparated interlayer excitons (IXs), where electrons and holes have their energy extrema in opposite layers. 1-5 Recently, IXs have been emerging as an exciting ground not only for exploring fascinating many-body phenomena, such as exciton condensation, 1-4 but also for realizing exciton-based information processing technologies.^{6,7} Formation of such IXs gives rise to photoluminescence (PL) emissions at lower energy with respect to intralayer excitons. In most heterobilayers such as MoSe₂/WSe₂, momentum-direct IXs located at K-valleys of constituent layers (K-K IX, Figure 1A) dominate the optical emission when the interlayer twist angles are small. 5,8-10 Spatial charge separation in such IXs results in significantly reduced oscillator strength and an inefficient PL emission. On the other hand, in certain heterobilayers such as MoS₂/WSe₂ and WS_2/MoS_2 , strong interlayer hybridization at the Γ -valley leads to Γ -K transition (Figure 1B) with enhanced oscillator strength. 11–17 However, bright PL emission is still hindered by its momentum-indirect nature.

While the emission properties of both momentum-direct K— K IX (emitting at \sim 1.0 eV) and momentum-indirect Γ -K IX (emitting at \sim 1.57 eV) have been investigated for MoS₂/WSe₂ HBLs, 16,18,19 effects of strain field and in-gap defect states on complex IX transitions remain to be understood. Particularly, by band-structure engineering, an electron residing in the sulfur-vacancy state ~200 meV below the MoS₂ conduction band edge²⁰ could be utilized to form optically active excitonic transition with a hole in the hybridized Γ band (Figure 1C).

This defect-bound Γ -band IX state (Γ -defect IX) retains the large oscillator strength of the hybridized Γ IX species. Owing to the deep trapping potential, the Γ -defect IX could enable high-purity quantum light generation in the technologically important yet rarely reached near-infrared (NIR) spectral range and elevate the operating temperature beyond the cryogenic regime.

To explore this potential, we fabricate nanopillars made of poly(methyl methacrylate) (PMMA), with the diameter of 150 nm and height of 200 nm, directly on a gold substrate. We then prepared three categories of heterostructures on top of the nanopillars/gold substrate: (i) MoS₂ /WSe₂ HBLs (also called HBLs for short, illustrated in Supporting Information Figure S1a); (ii) MoS₂ /WSe₂ HBL on top of a 5 nm hBN layer (HBL/hBN, illustrated in Figure S1b); (iii) bilayer-MoS₂/ monolayer-WSe2 (also called heterotrilayer, or HTL, illustrated in Figure S1c). Here nanopillars induce local strain within MoS_2/WSe_2 heterostructures. The hBN layer in sample category ii isolates the HBL from gold-induced fluorescence quenching and serves as a protective layer that shields the HBL from structural damages or substrate-induced adsorbates, hence defect generation, during the stamping process onto nanopillars. Since the Γ -valley features an out-of-plane orbital

Received: August 30, 2023 Revised: November 25, 2023 Accepted: November 28, 2023 Published: December 1, 2023





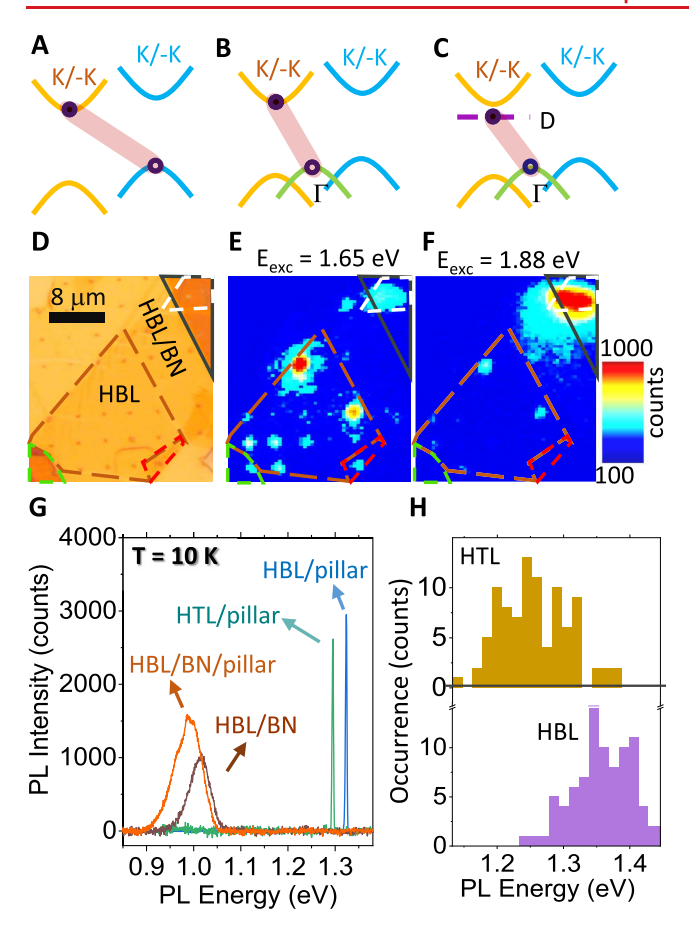


Figure 1. (A–C) Type-II band alignment of K–K IX (A), Γ–K IX (B), and Γ–defect IX (C). The excitons are indicated by pink ovals. (D) Optical image of an HBL flake on nanopillar arrays. Brown dashed line: HBL with 2° twist angle; white dashed line: HBL/hBN; black line: hBN flake; green line: $3L\text{-MoS}_2/1L\text{-WSe}_2$; red line: $2L\text{-MoS}_2/1L\text{-WSe}_2$ (HTL). (E and F) Wide-field PL image of panel D, under excitation wavelengths of 750 and 660 nm, respectively. (G) Typical NIR PL spectra of the HBL/nanopillar (blue), HTL/nanopillar (green), homogeneous HBL/hBN (brown), and HBL/hBN on the nanopillar (red). (H) Histograms of emission energies of HBL (violet) and HTL (brown) on nanopillars. Data were collected on six different samples at 10 K.

character, its orbital hybridization is sensitive to interlayer interactions. 11,17,25,26 For this reason, we stacked MoS $_2/WSe_2$ heterostructures with a near-zero or near-60° twist angle with $\pm 5^{\circ}$ error to achieve small layer separation 16 and strong interlayer interactions. 27,28 We developed a modified mechanical exfoliation method to efficiently create and transfer large (~100 μm) heterostructures (Supporting Information (SI) Section S1). Through Raman mapping, an average strain level of 0.38% was extracted from the Raman difference between the homogeneous HBL and the HBL on nanopillars (SI Section S2).

Under wide-field illumination at 750 nm wavelength, low-temperature PL images of the heterostructures were acquired by an InGaAs detector (Figure 1E and SI Section S3), revealing that NIR emitters are created at point-of-contact regions in HBL/nanopillars. Note that we use a gold substrate to quench the PL emission from the homogeneous HBL region and, thus, confine the IX emission at nanopillar sites. When switching excitation wavelengths from 750 to 660 nm (Figure 1F), the HBL/hBN region (Figure S1b and white box in

Figure 1D) becomes remarkably brighter, while the HBL/ nanopillars region (brown box in Figure 1D) significantly dims (explained later). Next, we spectrally resolve the HBL/ nanopillar emitters and find that the ~1.0 eV broad PL peak of K-K IX commonly reported in MoS2/WSe2 HBLs is replaced by narrow PL lines emerging mainly in the 1.35 \pm 0.08 eV range (Figure 1G,H), corresponding to a red shift distributed between 140 and 300 meV from the Γ-K IX emission energy at 1.57 eV.16 Since this energy red shift is in agreement with that of the sulfur-vacancy-induced PL red shift observed in MoS₂ monolayers, ^{20,29} we attribute the transition to Γ -defect IX formed between an electron trapped in the sulfur defect levels and a hole in the hybridized Γ band (the case in Figure 1C). For HTL/nanopillars, the energy of sharp PL lines is further red-shifted to the 1.26 \pm 0.1 eV range without significant reduction in PL intensity, advocating that we can utilize layer engineering as a tuning knob to control the Γ-defect IX emission range. (See SI Section S4 for more statistics and PL spectra). The sharp PL lines for both HBL and HTL samples are characterized with line widths of $\sim 1-5$ meV, comparable to those reported for WSe2 quantum emitters.^{23,2}

Interestingly, in the HBL/hBN region, where the hBN serves as a shielding layer minimizing defect generation and gold-induced PL quenching, a complete suppression of the Γ defect IX emission and recovery of the delocalized K-K IX transition at 1.0 eV is observed. Due to nanopillar strain, this emission exhibits a red shift and spectral broadening compared to that observed within unstrained regions (Figure 1G). This is consistent with recent studies reporting that narrow line width localized emissions cannot appear solely due to strain effect. 21,30 We also examined an HBL/nanopillar sample with 22° twist angle and found that the emission is significantly dimmer and shows a broader line width (SI Section S5). These findings provide evidence that control of twist angle, layer structure, defect concentration, and excitation wavelength can be utilized, along with nanoscale strain engineering, to achieve localization and activation of various IX transitions (see Table S1 for a summary).

To demonstrate that the Γ -defect IX can act as quantum emitters (QEs), we performed time-tagged, time-correlated photon counting and Hanbury-Brown-Tawiss (HBT) experiments at 10 K. Figure 2A shows the PL spectrum of a typical emitter, of which the spectrally filtered emission is guided into a two-channel single-photon detector to obtain a time-resolved PL (TRPL) curve (Figure 2C) and second-order photon correlation $(g^{(2)})$ trace (Figure 2D). Measured TRPL shows a lifetime of 18.45 \pm 0.01 ns, indicating that the line widths of narrow PL peaks, similar to those of other 2D QEs,²¹⁻²⁴ are significantly broader than the radiative decay limit. While a broad, non-transform-limited line width and a relatively long PL lifetime are generally not desirable, as they could limit the indistinguishability and generation rate of single photons, recent studies have demonstrated that it is possible to significantly reduce the lifetime, thereby outcompeting exciton dephasing, through the exploitation of plasmonic enhancement.31,32 Interestingly, the first few nanoseconds of the TRPL curve features a slow uprising from initial nonzero value. This is distinctly different from the TRPL curves of the K-K IX (Figure S10) showing monotonous decay, implying a delay between optical absorption and photocarrier recombination (explained later). The $g^{(2)}$ trace of this particular QE display almost complete photon antibunching with $g^{(2)}(0) = 0.01$ (our

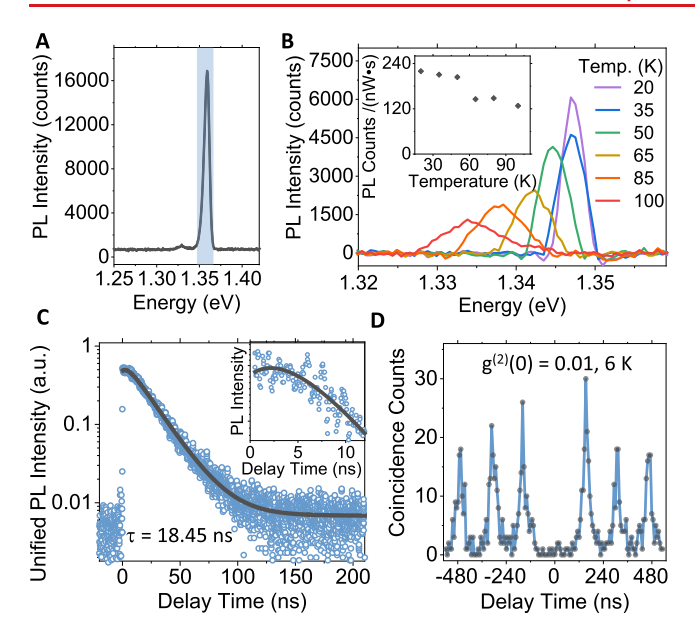


Figure 2. (A) PL spectrum of a localized HBL emitter on a nanopillar (data in panels B–D taken from this emitter with a band-pass filter that only allows the shadowed spectral region). (B) Temperature-dependent PL of a localized HBL emitter measured from 20 to 100 K. Inset: Evolution of integrated PL counts with temperature. (C) PL decay curve (blue) and theoretical fit to the data (black) with an 18.45 ± 0.01 ns lifetime. Inset: First 12 ns of the PL decay showing an uprising feature before the beginning of the single-exponential decay. (D) Second-order correlation measurement under 750 nm pulsed excitation with a 6.5 MHz repetition rate, showing $g^{(2)}(0) = 0.01$. Data were acquired at 10 K unless otherwise mentioned.

experimental sensitivity limit), indicating that it is possible to meet the strict requirement for implementation of quantum key distribution.³³ On the other hand, HBT experiments performed on other multiple QEs of HBL as well as HTL sample yield wider distribution of values below 0.5 (SI Section S6). These experiments together provide unequivocal con-

firmation of the single-photon nature of our Γ -defect IX. We attribute the single-photon emission to the fact that our QE is in complete spectral isolation from any of the intra- and interlayer excitonic transitions and the gold substrate effectively quenches the emission of the HBL except directly on top of the dielectric nanopillars. HBT experiment performed on a different emitter at 77 K reveals that the single-photon emission can sustain up to liquid nitrogen temperature (Figure S12b). The temperature-dependent PL experiment shows that while the PL lines get broader at elevated temperatures, the reduction of the integrated PL intensity is essentially insignificant (Figure 2B).

Next, to confirm the Γ -defect IX states as the physical origin of our QEs, we performed first-principles calculations on the electronic structures of the MoS₂/WSe₂ heterostructures. Compared with intrinsic HBL (Figure 3A), the band structure of strained HBL (Figure S14) shows that strain brings the Γ band closer in energy to the WSe₂ K valence band, facilitating the WSe₂ hole transfer. Note that the Γ band edge is dominated by the WSe₂ component (\sim 70%). When a sulfur vacancy is introduced, defect bands emerge below the conduction band minimum (CBM), in qualitative agreement with the red shift of Γ -defect IXs (Figure 3B). The introduction of Se vacancies, on the other hand, results in defect levels above the overall CBM of the HBL, leaving the low-energy optical transitions unchanged (SI Section S8). While the Γ band is highly hybridized and contains a substantial MoS₂ component, the VBM at the K-point only has contribution from the WSe₂ layer. As a result, excitons at the Γ -defect site exhibit a greater wave function overlap between the electron and hole compared to those at the Kvalley, leading to an enhanced oscillator strength (as illustrated in Figure 3C,D). These observations, in conjunction with the confinement of electrons at the sulfur-vacancy level, enable transitions at the Γ -defect site to dominate over those at the energetically favorable K-defect site. Further density functional theory (DFT) calculations detailing the evolution of band

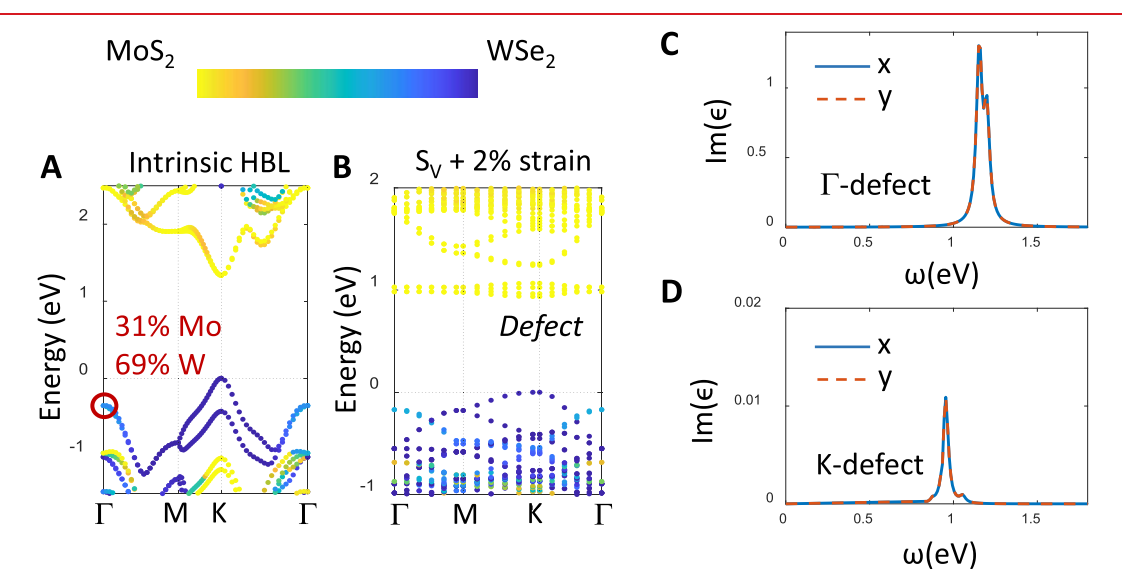


Figure 3. Band structures of (A) intrinsic MoS_2/WSe_2 HBL and (B) MoS_2/WSe_2 HBL with an S vacancy and 2% biaxial strain. Projected wave function components of individual layers are represented by the color bar. The percentages of MoS_2 and WSe_2 wave function at Γ band edge are displayed. Calculated dipole oscillator strengths of the 2% biaxial strained MoS_2/WSe_2 heterostructure with S-defect: (C) Γ-defect transition; (D) K-defect transition. The oscillator strengths of dipoles polarized along the x and y directions are both calculated, showing little polarization dependence.

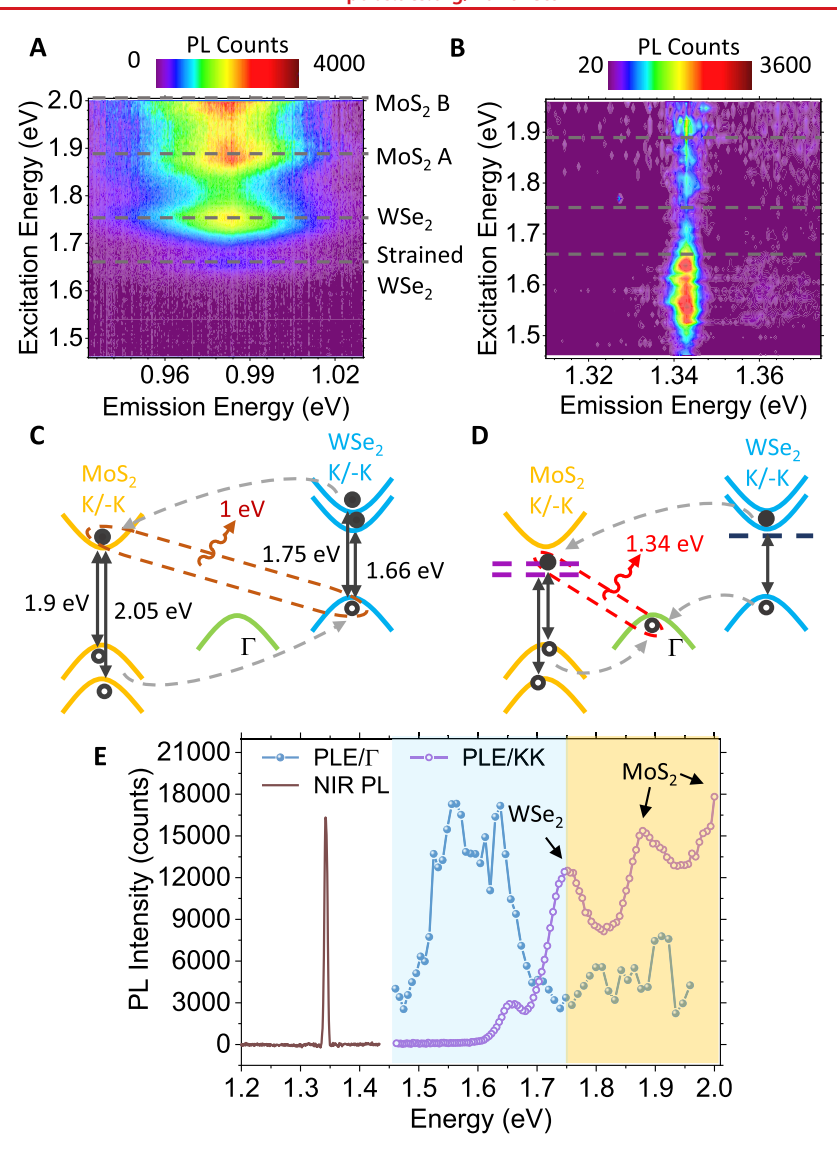


Figure 4. PLE maps as a function of both excitation and emission photon energies for a K-K IX emission (A) and for a Γ -defect IX emission (B) on a nanopillar, respectively. The energy of the intralayer excitons of each material is marked by gray dashed lines. Schematic representations of the energy band alignment in HBL/hBN on nanopillars (C) and HBL on nanopillars with defect bands (D). The black arrows show interband absorptions. The dashed gray arrows show charge transfer processes leading to the IX formations. The configurations for the K-K and Γ -defect IXs are represented by the dashed brown oval and the dashed red oval, respectively. (E) PL intensities at the K-K (purple line) and Γ -defect (blue line) IX peak as a function of excitation photon energy. The PL spectrum of the same Γ -defect IX emitter collected at near-infrared (brown line) spectral range is also shown. The spectral ranges of optical absorptions from WSe_2 -branch and MoS_2 -branch bound excitons are indicated by the blue and yellow shaded regions, respectively. Data were acquired at 10 K.

structures under varying strain and defect configurations are provided in SI Figures S14–S16.

Once an hBN layer is inserted between the HBL and nanopillars, defect formation in MoS_2 layer is averted as evidenced by the clean PL spectrum of the hBN encapsulated MoS_2 (Figure S17), and thus the K–K IX emission in the HBL is recovered. The room-temperature PL measurements further confirm that the momentum-indirect Γ –K emission in homogeneous HBL is replaced by the momentum-direct Γ -defect emission in HBL samples on nanopillars (Figure S18). Compared to HBL, the calculation for a HTL composed of bilayer MoS_2 and monolayer WSe_2 reveals a reduced band gap and an increased MoS_2 component at Γ -band maximum (Figure S16e), leading to further red-shifted NIR defect Γ -defect IX emissions (Figure 1H and Figure S7b) and enhanced MoS_2 -branch in PL excitation (PLE) spectra (SI Section S12).

Finally, to understand the strong influence of excitation wavelength on the competition between $K\!-\!K$ and $\Gamma\text{-defect }IX$ emissions, we conducted PLE experiments on three types of samples: (i) an HBL/hBN/nanopillar sample for probing K-K IX; (ii) HBL/nanopillar and (iii) HTL/nanopillar samples for probing Γ-defect IXs. For K-K IX emission, we observed enhanced PL intensity when the excitation is in resonance with delocalized 2D intralayer excitons (i.e., WSe₂ exciton at 1.75 eV as presented in Figure S19 and MoS2 A and B excitons at 1.88 and 2.01 eV, respectively), evidencing that the K-K IX is primarily formed by nonlocal interband absorption in constituent layers followed by interlayer charge transfer (Figure 4C). We also observed an absorption peak at 1.66 eV. We attributed this peak to absorption from strained WSe₂ region located on top of the pillar as strain has been shown to red shift the band-edge optical transitions. 12 This peak is much

weaker compared to that of the unstrained WSe₂ at 1.75 eV because carriers created in much larger unstrained WSe₂ region surrounding the nanopillar region are providing a major contribution to the K–K IX emission. In stark contrast, the Γ defect IX emitting at 1.34 eV from HBL/nanopillar shows a series of PLE peaks near the band edges of MoS₂ and WSe₂, predominantly in the 1.5 to 1.7 eV range (Figure 4B and Figure S20a). Considering their resemblance to the emissions from WSe₂ localized excitons, we attributed the PLE features in the 1.5 to 1.7 eV range to localized transitions that originate from the interband absorption of defect states in the WSe₂ layer amid local strain (Figure 4E, brown line). Such absorption patterns dominated by localized optical transitions were also observed in HTL/nanopillar samples (Figure S20b) but were not detected in HBL/hBN/nanopillar structures. Compared to HBLs, HTLs show enhanced PLE peaks near MoS₂ band edges due to an increased MoS₂ component at the Γ band edge (Figure S16e). Further discussions of the PLE measurements are provided in SI Section S12.

For Γ -defect IX emissions, HBL is coupled directly to the Au substrate except for the regions immediately above the nanopillars. As a result, only the excitons created in the nanopillar regions can contribute to the Γ -defect IX emissions, while all of the delocalized 2D intralayer excitons created in the vicinity of nanopillars were essentially quenched by gold. At nanopillar sites, excitons resonantly pumped into the 1.5-1.7 eV energy states are trapped by the strain-and-defect-induced potential wells before relaxing to the Γ -defect IX state. Therefore, absorption features of WSe₂ defect states were strongly enhanced relative to those of 2D intralayer excitons quenched by the gold layer. For K-K IX emissions from HBL/ hBN/nanopillars, the hBN spacer layer placed between the HBL and nanopillar arrays on gold substrate minimizes defect formation and suppresses the quenching of the 2D intralayer excitons. Therefore, 2D intralayer excitons formed in homogeneous HBL/hBN regions near the nanopillars could be funneled into the nearest nanopillar sites and contribute to the delocalized-exciton-dominated PLE features of the K-K IX emission in the absence of defect states. Taken together, these findings indicate that resonant excitation into WSe₂ localized exciton states as well as quenching of 2D intralayer excitons play a crucial role in defect- Γ IX quantum light emissions.

The fact that Γ -defect IXs are mainly populated via photoexcitation in WSe2 absorption bands may explain the slow uprising feature observed in the first few nanoseconds of the TRPL curve (Figure 2C and Figure S21). When the repetition rate of the pump laser is increased, the uprising feature becomes more pronounced due to the increase of carrier injection rate (SI Section S13). Such a slow rise suggests the slow arrival of holes to the hybridized Γ band. While the electron transfer from the CBM of WSe₂ to the Svacancy state is energetically downhill, the hole transfer from the K-point of WSe_2 to the hybridized Γ -point occurs uphill and requires an activation energy at low temperature. To get a better insight into the exciton photoexcited dynamics, a nonlinear rate equation model for the coupled K/–K exciton state in WSe₂ and Γ -defect IX is introduced in SI Section S13. The model successfully reproduces the initial time uprising feature in Figure 2C and yields a slow exciton transfer time of ~5 ns to the defect state. A good agreement was achieved (Figure S22a) between theory and experiment giving strong evidence toward validity of the proposed model (Figure 4D). Additionally, the model explains the long-time bunching

feature, in Figure 2D, which becomes more pronounced when extending the delay time to the μs time scale (Figure S22b). We attribute this bunching behavior to a dark defect shelving state receiving some portion of population from the Γ -defect IX on the time scale of 100 ns and repopulating back on the time scale of 2 μs . This observation suggests an additional complexity of the defect electronic states.

In summary, we show that strain, defect, layer engineering, and excitation energy can be utilized together to manipulate the IX formation in MoS₂/WSe₂ heterostructures for robust quantum light generation in the 1.15-1.45 eV NIR spectral range. In general, our approach unlocks the freedom of combining arbitrary 2D semiconductors for building IXs with desired emission energy and extending this strategy for engineering interfacial Γ-point transitions in other 2D heterostructures,³⁴ for instance, in MoS₂/WS₂. Given that monolayer TMDCs emit in the visible spectral range can be combined to generate IXs that emit in the NIR,35 our findings pave the way for extending the operational wavelength of 2D quantum light sources into the technologically important yet rarely reached NIR regime. Our strategy of creating sitecontrolled QEs from the defect-bound IXs signifies a paradigm shift in 2D quantum photonics research, moving from engineering intralayer exciton in monolayer structures toward IXs in 2D heterostructures.

ASSOCIATED CONTENT

Supporting Information

The Supporting Information is available free of charge at https://pubs.acs.org/doi/10.1021/acs.nanolett.3c03296.

Sample preparation; heterobilayer Raman spectrum; HBL PL image; additional PL spectra; emission property; additional TRPL and autocorrelation function data; comparison between localized Γ -defect IX and moire trapped IX; band-structure calculations; defect generation spectral evidence; additional PLE data; TRPL modeling of a QE; NIR SPEs comparison; optical measurement setup diagram (PDF)

AUTHOR INFORMATION

Corresponding Authors

Huan Zhao — Center for Integrated Nanotechnologies,
Materials Physics and Applications Division, Los Alamos
National Laboratory, Los Alamos, New Mexico 87545,
United States; Present Address: (H.Z.) Andrew and Peggy
Cherng Department of Medical Engineering, California
Institute of Technology, Pasadena, CA 91125, USA;
orcid.org/0000-0002-4982-0865; Email: hzhao06@
gmail.com

Li Yang — Department of Physics, Washington University in St. Louis, Missouri 63130, United States; Institute of Materials Science and Engineering, Washington University in St. Louis, Missouri 63130, United States; orcid.org/0000-0002-8611-6359; Email: lyang@physics.wustl.edu

Han Htoon — Center for Integrated Nanotechnologies, Materials Physics and Applications Division, Los Alamos National Laboratory, Los Alamos, New Mexico 87545, United States; oorcid.org/0000-0003-3696-2896; Email: htoon@lanl.gov Nano Letters pubs.acs.org/NanoLett Letter

Authors

- Linghan Zhu Department of Physics, Washington University in St. Louis, Missouri 63130, United States; orcid.org/0000-0002-9259-5077
- Xiangzhi Li Center for Integrated Nanotechnologies, Materials Physics and Applications Division, Los Alamos National Laboratory, Los Alamos, New Mexico 87545, United States; Oorcid.org/0000-0002-7117-4513
- Vigneshwaran Chandrasekaran Center for Integrated Nanotechnologies, Materials Physics and Applications Division, Los Alamos National Laboratory, Los Alamos, New Mexico 87545, United States; orcid.org/0000-0002-6014-9953
- Jon Kevin Baldwin Center for Integrated Nanotechnologies, Materials Physics and Applications Division, Los Alamos National Laboratory, Los Alamos, New Mexico 87545, United States
- Michael T. Pettes Center for Integrated Nanotechnologies, Materials Physics and Applications Division, Los Alamos National Laboratory, Los Alamos, New Mexico 87545, United States; o orcid.org/0000-0001-6862-6841
- Andrei Piryatinski Center for Integrated Nanotechnologies, Materials Physics and Applications Division, Los Alamos National Laboratory, Los Alamos, New Mexico 87545, United States; Theoretical Division, Los Alamos National Laboratory, Los Alamos, New Mexico 87545, United States; orcid.org/0000-0001-9218-1678

Complete contact information is available at: https://pubs.acs.org/10.1021/acs.nanolett.3c03296

Author Contributions

H.Z., under the supervision of H.H., conceived, designed, and conducted the experiment and analyzed the data. L.Z. and L.Y. performed first-principles calculations. M.T.P. conducted Raman measurements. X.L. and V.C. assisted H.Z. in PL measurements. J.K.B. assisted in sample preparation. A.P. performed the modeling of the TRPL and photon correlation function. H.Z. and H.H. wrote the manuscript with input from all the authors. All authors have given approval to the final version of the manuscript.

Notes

The authors declare no competing financial interest.

ACKNOWLEDGMENTS

This work was performed at the Center for Integrated Nanotechnologies, an Office of Science User Facility operated for the U.S. Department of Energy (DOE), Office of Science, by Los Alamos National Laboratory (LANL). H.Z., X.L., and H.H. acknowledge the primary support by Quantum Science Center, a National Quantum Information Science Research Center supported by Office of Science, U.S. DOE. V.C. is supported by DOE BES Program BES LANL22. A.P. acknowledges support from the Laboratory Directed Research and Development (LDRD) program 20200104DR. M.T.P. is supported by LDRD 20210782ER and LDRD 20210640ECR. H.Z. also acknowledges a LANL Director's Postdoctoral Fellow Award. L.Z. is supported by the National Science Foundation (NSF) Grant No. DMR-2124934, and L.Y. is supported by the Air Force Office of Scientific Research (AFOSR) Grant No. FA9550-20-1-0255. The first-principles simulation uses Anvil at Purdue University through allocation DMR100005 from the Advanced Cyberinfrastructure Coordination Ecosystem: Services & Support (ACCESS) program, which is supported by NSF grants #2138259, #2138286, #2138307, #2137603, and #2138296.

REFERENCES

- (1) Huang, D.; Choi, J.; Shih, C.-K.; Li, X. Excitons in semiconductor moiré superlattices. *Nat. Nanotechnol.* **2022**, 1–12.
- (2) Wilson, N. P.; Yao, W.; Shan, J.; Xu, X. Excitons and emergent quantum phenomena in stacked 2D semiconductors. *Nature* **2021**, 599 (7885), 383–392.
- (3) Jiang, Y.; Chen, S.; Zheng, W.; Zheng, B.; Pan, A. Interlayer exciton formation, relaxation, and transport in TMD van der Waals heterostructures. *Light. Sci. Appl.* **2021**, *10* (1), 72.
- (4) Rivera, P.; Yu, H.; Seyler, K. L.; Wilson, N. P.; Yao, W.; Xu, X. Interlayer valley excitons in heterobilayers of transition metal dichalcogenides. *Nat. Nanotechnol.* **2018**, *13* (11), 1004–1015.
- (5) Rivera, P.; Schaibley, J. R.; Jones, A. M.; Ross, J. S.; Wu, S.; Aivazian, G.; Klement, P.; Seyler, K.; Clark, G.; Ghimire, N. J. Observation of long-lived interlayer excitons in monolayer MoSe2—WSe2 heterostructures. *Nat. Commun.* **2015**, *6* (1), 6462.
- (6) Turunen, M.; Brotons-Gisbert, M.; Dai, Y.; Wang, Y.; Scerri, E.; Bonato, C.; Jöns, K. D.; Sun, Z.; Gerardot, B. D. Quantum photonics with layered 2D materials. *Nat. Rev. Phys.* **2022**, 219–236.
- (7) Baek, H.; Brotons-Gisbert, M.; Koong, Z. X.; Campbell, A.; Rambach, M.; Watanabe, K.; Taniguchi, T.; Gerardot, B. D. Highly energy-tunable quantum light from moiré-trapped excitons. *Sci. Adv.* **2020**, *6* (37), No. eaba8526.
- (8) Förg, M.; Baimuratov, A. S.; Kruchinin, S. Y.; Vovk, I. A.; Scherzer, J.; Förste, J.; Funk, V.; Watanabe, K.; Taniguchi, T.; Högele, A. Moiré excitons in MoSe2-WSe2 heterobilayers and heterotrilayers. *Nat. Commun.* **2021**, *12* (1), 1656.
- (9) Tran, K.; Moody, G.; Wu, F.; Lu, X.; Choi, J.; Kim, K.; Rai, A.; Sanchez, D. A.; Quan, J.; Singh, A. Evidence for moiré excitons in van der Waals heterostructures. *Nature* **2019**, *567* (7746), 71–75.
- (10) Seyler, K. L.; Rivera, P.; Yu, H.; Wilson, N. P.; Ray, E. L.; Mandrus, D. G.; Yan, J.; Yao, W.; Xu, X. Signatures of moiré-trapped valley excitons in MoSe2/WSe2 heterobilayers. *Nature* **2019**, *567* (7746), 66–70.
- (11) Tebyetekerwa, M.; Zhang, J.; Saji, S. E.; Wibowo, A. A.; Rahman, S.; Truong, T. N.; Lu, Y.; Yin, Z.; Macdonald, D.; Nguyen, H. T. Twist-driven wide freedom of indirect interlayer exciton emission in MoS2/WS2 heterobilayers. *Cell Rep. Phys. Sci.* **2021**, 2 (8), 100509.
- (12) Cho, C.; Wong, J.; Taqieddin, A.; Biswas, S.; Aluru, N. R.; Nam, S.; Atwater, H. A. Highly strain-tunable interlayer excitons in MoS2/WSe2 heterobilayers. *Nano Lett.* **2021**, *21* (9), 3956–3964.
- (13) Ren, L.; Li, L.; Lv, Y.; Li, X.; Zhang, D.; Li, W.; Liu, L.; Kong, L.; Duan, X.; Wang, X.; Pan, A.; Liao, L.; Liu, Y. Efficient modulation of MoS2/WSe2 interlayer excitons via uniaxial strain. *Appl. Phys. Lett.* **2022**, 120 (5), 053107.
- (14) Unuchek, D.; Ciarrocchi, A.; Avsar, A.; Watanabe, K.; Taniguchi, T.; Kis, A. Room-temperature electrical control of exciton flux in a van der Waals heterostructure. *Nature* **2018**, *560* (7718),
- (15) Okada, M.; Kutana, A.; Kureishi, Y.; Kobayashi, Y.; Saito, Y.; Saito, T.; Watanabe, K.; Taniguchi, T.; Gupta, S.; Miyata, Y. Direct and indirect interlayer excitons in a van der Waals heterostructure of hBN/WS2/MoS2/hBN. ACS Nano 2018, 12 (3), 2498–2505.
- (16) Kunstmann, J.; Mooshammer, F.; Nagler, P.; Chaves, A.; Stein, F.; Paradiso, N.; Plechinger, G.; Strunk, C.; Schüller, C.; Seifert, G. Momentum-space indirect interlayer excitons in transition-metal dichalcogenide van der Waals heterostructures. *Nat. Phys.* **2018**, *14* (8), 801–805.
- (17) Heo, H.; Sung, J. H.; Cha, S.; Jang, B.-G.; Kim, J.-Y.; Jin, G.; Lee, D.; Ahn, J.-H.; Lee, M.-J.; Shim, J. H. Interlayer orientation-dependent light absorption and emission in monolayer semiconductor stacks. *Nat. Commun.* **2015**, *6* (1), 7372.

- (18) Tan, Q.; Rasmita, A.; Li, S.; Liu, S.; Huang, Z.; Xiong, Q.; Yang, S. A.; Novoselov, K.; Gao, W.-b. Layer-engineered interlayer excitons. *Sci. Adv.* **2021**, *7* (30), No. eabh0863.
- (19) Karni, O.; Barré, E.; Lau, S. C.; Gillen, R.; Ma, E. Y.; Kim, B.; Watanabe, K.; Taniguchi, T.; Maultzsch, J.; Barmak, K. Infrared interlayer exciton emission in MoS 2/WSe 2 heterostructures. *Phys. Rev. Lett.* **2019**, 123 (24), 247402.
- (20) Mitterreiter, E.; Schuler, B.; Micevic, A.; Hernangómez-Pérez, D.; Barthelmi, K.; Cochrane, K. A.; Kiemle, J.; Sigger, F.; Klein, J.; Wong, E. The role of chalcogen vacancies for atomic defect emission in MoS2. *Nat. Commun.* **2021**, *12* (1), 3822.
- (21) Parto, K.; Azzam, S. I.; Banerjee, K.; Moody, G. Defect and strain engineering of monolayer WSe2 enables site-controlled single-photon emission up to 150 K. *Nat. Commun.* **2021**, *12* (1), 3585.
- (22) Zhao, H.; Pettes, M. T.; Zheng, Y.; Htoon, H. Site-controlled telecom-wavelength single-photon emitters in atomically-thin MoTe2. *Nat. Commun.* **2021**, *12* (1), 6753.
- (23) Palacios-Berraquero, C.; Kara, D. M.; Montblanch, A. R.-P.; Barbone, M.; Latawiec, P.; Yoon, D.; Ott, A. K.; Loncar, M.; Ferrari, A. C.; Atatüre, M. Large-scale quantum-emitter arrays in atomically thin semiconductors. *Nat. Commun.* **2017**, *8* (1), 15093.
- (24) Branny, A.; Kumar, S.; Proux, R.; Gerardot, B. D. Deterministic strain-induced arrays of quantum emitters in a two-dimensional semiconductor. *Nat. Commun.* **2017**, *8* (1), 15053.
- (25) Tongay, S.; Fan, W.; Kang, J.; Park, J.; Koldemir, U.; Suh, J.; Narang, D. S.; Liu, K.; Ji, J.; Li, J. Tuning interlayer coupling in large-area heterostructures with CVD-grown MoS2 and WS2 monolayers. *Nano Lett.* **2014**, *14* (6), 3185–3190.
- (26) Komsa, H.-P.; Krasheninnikov, A. V. Electronic structures and optical properties of realistic transition metal dichalcogenide heterostructures from first principles. *Phys. Rev. B* **2013**, 88 (8), 085318
- (27) Susarla, S. M.; Sassi, L.; Zobelli, A.; Woo, S. Y.; Tizei, L. H.; Stéphan, O.; Ajayan, P. M. Mapping Modified Electronic Levels in the Moiré Patterns in MoS2/WSe2 Using Low-Loss EELS. *Nano Lett.* **2021**, *21* (9), 4071–4077.
- (28) Alexeev, E. M.; Ruiz-Tijerina, D. A.; Danovich, M.; Hamer, M. J.; Terry, D. J.; Nayak, P. K.; Ahn, S.; Pak, S.; Lee, J.; Sohn, J. I. Resonantly hybridized excitons in moiré superlattices in van der Waals heterostructures. *Nature* **2019**, *567* (7746), 81–86.
- (29) Klein, J.; Sigl, L.; Gyger, S.; Barthelmi, K.; Florian, M.; Rey, S.; Taniguchi, T.; Watanabe, K.; Jahnke, F.; Kastl, C. Engineering the luminescence and generation of individual defect emitters in atomically thin MoS2. ACS Photonics 2021, 8 (2), 669–677.
- (30) Wang, W.; Ma, X. Strain-induced trapping of indirect excitons in MoSe2/WSe2 heterostructures. *ACS Photonics* **2020**, 7 (9), 2460–2467.
- (31) Luo, Y.; Shepard, G. D.; Ardelean, J. V.; Rhodes, D. A.; Kim, B.; Barmak, K.; Hone, J. C.; Strauf, S. Deterministic coupling of site-controlled quantum emitters in monolayer WSe2to plasmonicnanocavities. *Nat. Nanotechnol* **2018**, *13*, 1137–1142.
- (32) Luo, Y.; He, X.; Kim, Y.; Blackburn, J. L.; Doorn, S. K.; Htoon, H.; Strauf, S. Carbon Nanotube Color Centers in PlasmonicNanocavities: A path to photon indistinguishability at telecom bands. *Nano Lett.* **2019**, *19*, 9037.
- (33) Aharonovich, I.; Englund, D.; Toth, M. Solid-state single-photon emitters. *Nat. Photon* **2016**, *10* (10), 631–641.
- (34) Ubrig, N.; Ponomarev, E.; Zultak, J.; Domaretskiy, D.; Zólyomi, V.; Terry, D.; Howarth, J.; Gutiérrez-Lezama, I.; Zhukov, A.; Kudrynskyi, Z. R. Design of van der Waals interfaces for broadspectrum optoelectronics. *Nat. Mater.* **2020**, *19* (3), 299–304.
- (35) Chaves, A.; Azadani, J. G.; Alsalman, H.; da Costa, D. R.; Frisenda, R.; Chaves, A. J.; Song, S. H.; Kim, Y. D.; He, D.; Zhou, J.; Castellanos-Gomez, A.; Peeters, F. M.; Liu, Z.; Hinkle, C. L.; Oh, S.-H.; Ye, P. D.; Koester, S. J.; Lee, Y. H.; Avouris, Ph.; Wang, X.; Low, T. Bandgap Engineering of Two-Dimensional Semiconductor Materials. *npj* 2D Mater. Appl. 2020, 4 (1), 29.